

Scale Collapse of Vortices at Porous-Fluid Interfaces

Justin Courter, Vishal Srikanth, Thibaut Kemayo, and Andrey V. Kuznetsov ^{*}

Department of Mechanical and Aerospace Engineering, North Carolina State University, Raleigh, NC 27695, USA

The interaction between externally generated turbulence and porous media is central to many engineering and environmental flows, yet the fate of macroscale vortical structures at a porous/fluid interface remains uncharacterized. By numerically simulating the turbulent flow, we investigate the penetration, breakdown, and turbulence kinetic energy (TKE) transport of macroscale vortices impinging on porous matrices with high porosities $\phi = 0.80\text{--}0.95$. For all porosities considered, macroscale vortices collapse abruptly at the porous interface and do not persist within the matrix, supporting the pore-scale prevalence of turbulence even under strong external forcing. Although vortex impingement injects TKE into the porous medium through turbulent transport at the interface, this supplied TKE is rapidly redistributed and dissipated as the flow reorganizes to satisfy pore-scale geometric constraints. Deeper within the porous layer, turbulence is sustained primarily by local shear production associated with pore-scale velocity gradients, and the internal flow becomes increasingly independent of upstream conditions. Variations in porosity modulate the relative balance between production and dissipation by altering geometric confinement and effective Reynolds number, but the dominant turbulent length scale within the porous matrix remains set by the pore size. These results demonstrate that porous media act as a robust geometric filter that enforces pore-scale-dominated turbulence regardless of external forcing.

Keywords: Turbulent vortex impingement; Porous media momentum transport; Direct Numerical Simulation (DNS); Momentum and energy transport; turbulent kinetic energy

1 Introduction

Understanding vortex-penetration dynamics and the TKE budget at the entrance of and within porous media is crucial for applications ranging from filtration (Rajagopalan & Tien 1976) and predictive porous-flow models to industrial transport control (Hanspal *et al.* 2013) where the flow dynamics at the interface between a free flow and porous region impact the mass and heat transfer. It is also applicable to natural hazards such as wildfire propagation (Mell *et al.* 2009), where vegetation layers govern enhanced turbulent mixing and flame spread. Porous layers may also be used as a drag reduction mechanism (Abderrahaman-Elena & García-Mayoral 2017) where porous layers increase or reduce drag by greater than 20% (Rosti *et al.* 2018) by increasing or reducing the anisotropic permeability of the porous layer. In aerodynamics, porous layers can be used on a wind turbine blade surface to enhance aerodynamic

^{*} Email address for correspondence: avkuznet@ncsu.edu

performance (Zamani *et al.* 2021). This drag reduction property also exists, for example, on a seal fur surface where a drag reduction ratio was noted to be 12% for a glycerol-water mixture in (Itoh *et al.* 2006).

Porous coatings are also applicable to thermal management and heat transfer optimization in systems such as gas turbines, industrial scale heat exchangers, or electronics cooling (Zhao & Lu 2002). For example, (Huang *et al.* 2022), (Chu *et al.* 2019) found that the vortex shedding and secondary flow instabilities inherent in microscale vortices generated by a porous matrix significantly influence the Nusselt number, and (Chen *et al.* 2025) found that jet impingement onto a porous lattice increases heat transfer by up to 110%. The impingement mechanism onto a porous matrix and the development of the flow within the porous matrix can greatly impact both the heat transfer characteristics and the fluid dynamics. Experimental evidence of turbulent flow in porous media is reported in (Mayer 2014), where a sharp increase in the pressure loss in a porous layer when increasing the Reynolds number was found and attributed to turbulent flow (see Fig. 3.7 in (Mayer 2014)). Although the impact of externally generated turbulence on porous media has been studied for decades by the likes of (Suga *et al.* 2010) and (Manes *et al.* 2011) which investigated the impact of wall permeability on turbulence, most work emphasizes idealized periodic media or partially porous channel flows in which intralayer motion is often laminar. Turbulent motions with length scales larger than the pore spacing are referred to as *macroscale*, whereas motions with smaller length scales are referred to as *microscale*. Consequently, the fate of macroscale vortices at the interface remains unresolved.

(Rao & Jin 2022) define porous media as a material type which possesses both a solid matrix and interconnected voids. Even though the interaction at a porous/clear-fluid interface is unclear, the previous debate on the possibility of macroscale turbulence in a porous media has been settled. There were those who held that macroscale turbulence could survive in a porous media and those who held that it could not because of geometric constraints placed on the eddies by the porous obstacles. (Jin *et al.* 2015) found that eddy size is limited to the distance between pores which suggested that the latter view was correct; this view is known as the pore scale prevalence hypothesis (PSPH). (Uth *et al.* 2016) and (Jin & Kuznetsov 2017) confirmed the PSPH for different geometries using DNS. (He *et al.* 2019), (He *et al.* 2018), and (Chu *et al.* 2018) further solidified the view that porous media inherently limit the time and length scale of turbulence in porous media via pore-size constraints, which suppress the development of large-scale vortices within the matrix. There is likely a porosity greater than 98% in which the flow constraints are sufficiently nonlimiting that macroscale turbulent structures are allowed to exist (Rao & Jin 2022). The maximum velocity is limited here to $\phi=0.95$ to combat this effect and ensure the porous medium sufficiently constrains the impinging flow. The vortices which are allowed to exist within the porous matrix are known as microscale vortices, and they tend to form downstream of individual pores which make up the porous matrix (Srikanth & Kuznetsov 2025). The vortices are eventually advected to the free stream region between the pores where they are eventually dissipated. These studies, along with (Härter *et al.* 2023) and (Chu *et al.* 2021), link porosity to turbulent flow organization, interfacial coupling and, in some cases, drag and heat-transfer metrics such as drag coefficients or Nusselt numbers.

Externally generated turbulence can introduce large vortices at the porous–fluid interface. Few studies have focused on externally generated turbulence in the past. (Hao & García-Mayoral 2025) found that substrate permeability is the dominant parameter controlling drag, slip, and turbulence over porous and rough walls. (Kuwata & Suga 2019) found that varying wall permeability modifies the friction drag, the characteristic turbulent length scales near the porous interface, and the thickness of the turbulent boundary layer on the porous-wall side. (Rosti *et al.* 2018) found that high wall permeabilities allow turbulent eddies

from the clear fluid region to penetrate far into the porous matrix while low permeabilities damp the turbulent structures within the first few obstacles. Since the interaction of macroscale vortices and a porous matrix is still a developing area of research, we explore how macroscale vortices behave upon striking the porous layer and how their length scale evolves as they penetrate the medium. We particularly focus on the transport of TKE because the extent to which a vortex retains coherent structure as it advances into the layer is determined by the TKE budget—production, transport, pressure diffusion, viscous diffusion, and dissipation—governing both dynamics and spatial distribution of TKE across the medium. This TKE budget-based perspective clarifies how external forcing reorganizes interfacial production, turbulent and pressure diffusion, and dissipation within pore-scale pathways.

A Direct Numerical Simulation (DNS) framework is employed to simulate the turbulent wake generated by a single solid obstacle impinging on a downstream porous layer at a fixed inlet Reynolds number set by the upstream velocity condition. DNS simulations do not require turbulence modelling of any kind, so they are the only fully resolved numerical models which can answer whether macroscopic turbulence can exist in porous matrices (Jin *et al.* 2015), (Uth *et al.* 2016), (Rao & Jin 2022). Within the porous layer, the pore scale Reynolds number depends on porosity through the pore size and the local velocity in the passages. The full TKE budget—from production to dissipation—is evaluated to elucidate the dynamics of vortex penetration and energy transfer (spatial transport and cascade). The porous medium is modeled as a two-dimensional array of microscale solid obstacles in an in-line configuration. For each porosity, simulations are advanced to a statistically stationary state, and the time-averaged velocity components are recorded to calculate the turbulent length scale within the porous medium (i) downstream of the bluff body, (ii) at the porous-fluid interface, and (iii), at the mid plane within the porous matrix. Each term within the TKE transport equation is also calculated once the solution has reached a statistically steady state.

2 Numerical Methods

In this paper, we investigate the turbulent flow inside a porous domain composed of square solid obstacles. Five cases are simulated in total; four cases include a large bluff body upstream of the porous domain, whose purpose is to introduce macroscale turbulence into the flow. The porosities of the porous region are $\phi = 0.80, 0.85, 0.90$, and 0.95 . Another case is simulated with a porosity $\phi = 0.85$ without a bluff body upstream of the porous domain, so that no macroscale vortex impingement on the porous matrix occurs; this case isolates the impact of the porous matrix on TKE transport and provides a baseline against which the effects of vortex impingement can be compared.

Figure 1 shows the two-dimensional macroscale domain with a flow inlet on the left and an outlet on the right. An incoming uniform free stream flow first encounters a single bluff body (large, square obstacle) placed upstream of a porous layer modeled as a two-dimensional, in-line array of pore-scale solid obstacles. The bluff-body size far exceeds the pore size, establishing the relevant scale separation. The standoff distance between the bluff body and the front face of the porous layer allows the wake to develop before impingement. The layer occupies a finite streamwise section roughly in the middle of the channel, and a downstream region enables observation of post-exit wake evolution. This configuration resolves the interaction of the macroscale bluff-body wake with the porous–fluid interface, including penetration over several rows of microscale solid obstacles in the porous layer.

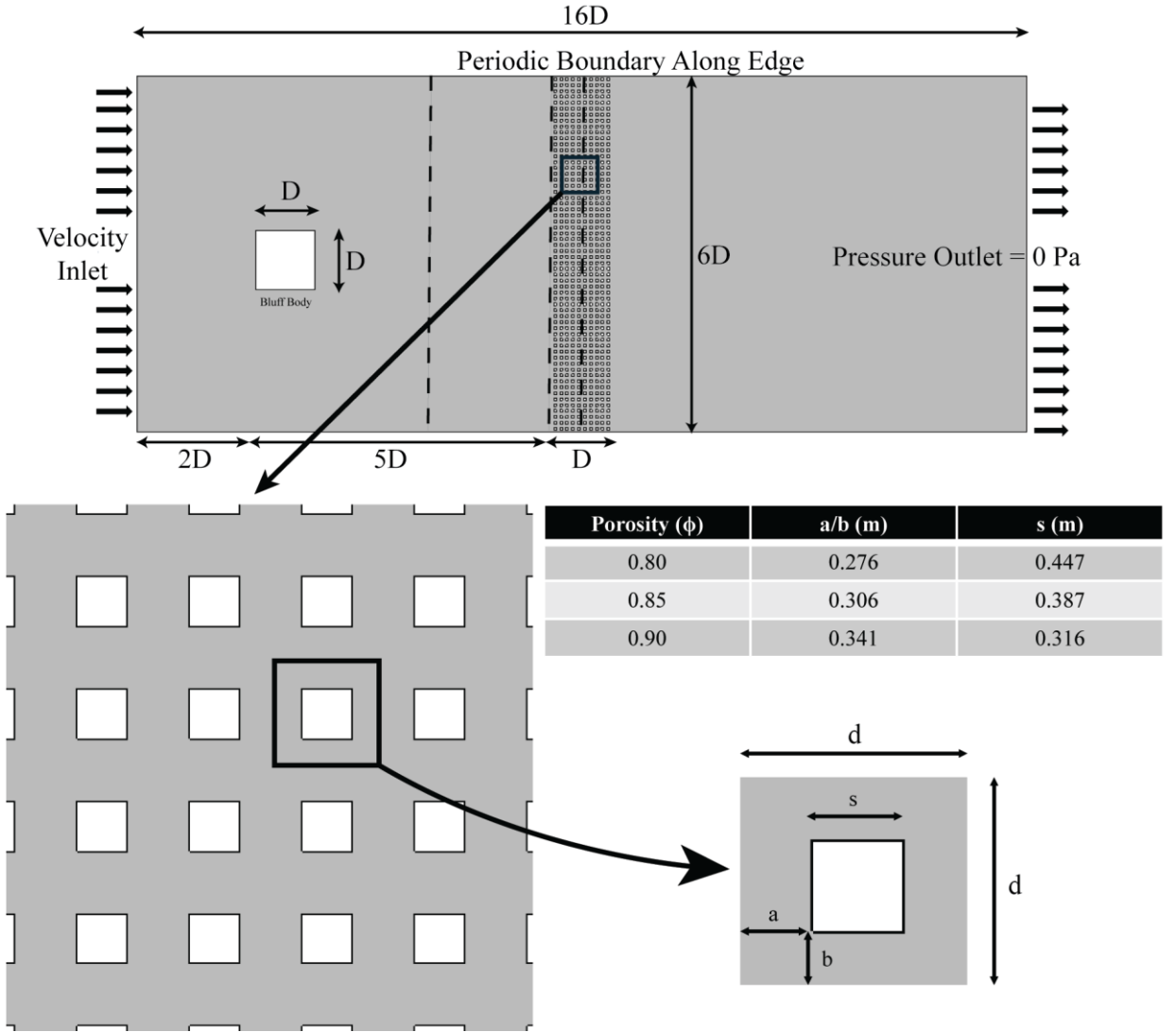


Figure 1: The representative geometry with uniform flow at the inlet, a square bluff body of side D placed $2D$ from the inlet, and the porous domain placed $5D$ downstream from the bluff body. The porous matrix has 600 total porous obstacles (10×60). The top and bottom are periodic boundary conditions, and the outlet is a pressure outlet. The dashed lines correspond to the locations where the correlation functions are computed: (i) midway between the bluff body and porous matrix, (ii) at the clear fluid/porous interface, and (iii) within the porous matrix.

The velocity at the domain inlet, the fluid properties, and the large solid obstacle side lengths are set such that the macroscale Reynolds number at the large solid obstacle has a value of 10,000 where the Reynolds number is calculated as:

$$Re = \frac{\rho u_{in} D}{\mu} \quad (1)$$

where u_{in} is the inlet velocity, ρ is the fluid density, μ is the fluid viscosity, and D is the side of the large solid obstacle, and the characteristic length scale of the region upstream of the porous domain. u_{in} , ρ ,

μ , and D are valued a 1 m/s, 1 kg/m³, 0.001 Pa·s, and 10 m, respectively, which sets the Reynolds number to 10,000.

Porosity is defined as the area occupied by pores over the total area within the porous domain:

$$\phi = \frac{V_{void}}{V_{total}} \quad (2)$$

where V_{void} is the volume occupied by voids and V_{total} is the total volume of the porous domain (including both obstacles and voids).

The porosity is varied by assuming a repeating, square characteristic area within the porous domain. The characteristic length scale in the porous domain is defined as the distance between porous obstacles which is equivalent to a size of d and a characteristic area of d^2 . There are a total of 600 repeated areas which constitute the whole of the porous domain; 10 instances patterned streamwise and 60 patterned cross-stream for a total porous domain area of $600d^2$. The desired porosity is varied by changing the size of the solid obstacle within the porous domain while retaining the characteristic area constant and spacing between pore midlines constant.

$$\phi = 1 - \left(\frac{s}{d}\right)^2 \quad (3)$$

ANSYS Fluent 21.2 was used to solve the DNS governing equations. A Coupled scheme was used for the Pressure-Velocity Coupling, a Least Squares Cell Based spatial discretization was used for the gradient, PRESTO! was used to solve for pressure, QUICK was used to solve for momentum, and Second Order Implicit was used for the transient formulation. Each simulation was first monitored using the drag coefficient to verify stable solver behavior and initial convergence. After the drag monitor stabilized, a root-mean-square x -velocity (RMSE) monitor was used to confirm that the solution had reached a statistically steady state. Simulations were performed in ANSYS Fluent on North Carolina State University's Hazel HPC cluster using 40 CPU cores. A representative case ($\phi = 0.80$) used a mesh of 1,115,048 nodes and was advanced with a time step of $\Delta t = 0.05$ until statistical stationarity was achieved; the total wall-clock runtime was approximately 6.46 days. It was assumed that once variations in RMSE were deemed negligible and there was no clear trend in the fluctuations in time, the simulation had reached a statistically steady state. Once the simulation was statistically stationary, additional x -velocity monitors were implemented along the cross-flow direction at 3 different locations: downstream of the large solid obstacle, at the porous interface, and midway through the porous domain, as exhibited in Figure 1.

The data collected at each location was used to calculate a spatial correlation function to quantify the size of coherent turbulent structures. The spatial correlation can be calculated using:

$$R(dy, y_0) = \frac{\langle u'(y_0, t) \cdot u'(y_0 + dy, t) \rangle_t}{\langle u'^2(y_0, t) \rangle_t} \quad (4)$$

where the reference point, y_0 , for the correlation function is at the midpoint along the cross-stream line, and the x -velocity data are used in the correlation function calculation until the correlation function does not significantly change with additional data. r_{uu} is the correlation function, which is normalized with respect to the reference location, the $\langle \cdot \rangle_t$ operator denotes time averaging, and u' is the

fluctuating component of x -velocity. It was also confirmed that the correlations exhibited at all locations within the domain are not geometrically induced. To prove this, the correlation in time was computed with a sufficiently large time separation using:

$$\tilde{R}(dy, y_0, d\tau, \tau) = \frac{\langle u'(y_0, \tau) \cdot u'(y_0 + dy, \tau + d\tau) \rangle_t}{\langle u'^2(y_0, \tau) \rangle_t} \quad (5)$$

The correlation function at time $\tau + d\tau$ was then subtracted from the spatial function to determine the fluctuation components which were truly turbulent:

$$\hat{R}(dy, y_0) = R(dy, y_0) - \tilde{R}(dy, y_0, d\tau, \tau) \quad (6)$$

Since the correlation at time $\tau + d\tau$ is essentially negligible relative to the spatial correlation function, the truly turbulent components are the same as the spatial correlation function. That is:

$$\hat{R}(dy, y_0) \approx R(dy, y_0) \quad (7)$$

Therefore, it was concluded that the correlations confirm truly random fluctuations as opposed to periodic fluctuations such as the unsteady laminar vortex oscillations behind bluff bodies. Finally, each term in the TKE budget is volume averaged within the porous domain over each characteristic area.

The governing equations and details of the DNS models used are included in Appendix A, the derivation of the TKE terms are included in Appendix B, the validation of the model against experimental results is detailed in Appendix C, and a grid resolution study is presented in Appendix D. The density, velocity, pore size, and viscosity are selected such that the governing equations are non-dimensional. Therefore, the subsequent results reported in the following sections are scaled so that they are non-dimensional as well.

In order to resolve the microscale turbulence structures at a feasible computational cost, the geometry is assumed to be 2D, similar to prior studies that employed 2D simulation models to resolve turbulence and develop fundamental scaling behaviors (Blackburn & Lopez 2003; Chen & Wu 2024; Gasow *et al.* 2020; Hewitt *et al.* 2012). The objective of this study is to develop a theoretical, qualitative understanding of how macroscale vortices interact with the microscale pores of a porous layer. To this end, we employ the 2D approximation as a theoretical limit, isolating the dynamics of coherent structures from stochastic background turbulence. We acknowledge that 2D DNS inherently neglects the vortex stretching mechanism essential for the forward energy cascade in 3D flows. While this omission prevents the prediction of realistic vortex breakdown, it enables a rigorous characterization of the fundamental shedding modes and their interaction with pore boundaries.

Consequently, we anticipate a prolonged survival of large-scale eddies in 2D turbulence compared to 3D. Precise quantitative predictions of drag are outside the scope of this work. Instead, turbulence statistics are interpreted via the Kraichnan-Leith-Batchelor theory of 2D turbulence. In this framework, TKE values represent the energy stored in the large-scale coherent vortices. TKE production serves as a theoretical maximum for energy transfer from the mean shear, free from spanwise losses. Finally, the dissipation rate is interpreted as entropy dissipation, representing the viscous smoothing of vorticity gradients rather than kinetic energy loss. This framework establishes a limiting scenario for vortex

persistence. If macroscale structures are attenuated in this 2D limit, they would undoubtedly be destroyed in a fully 3D environment.

3 Results and Discussion

Interaction of turbulent flow in porous media with external boundaries is a vital problem in practical applications and yet it remains a poorly characterized phenomenon. The goal of this study is to understand the transport mechanism of macroscale turbulent vortices when they are externally forced perpendicular to a porous/clear fluid interface. To characterize this fundamental phenomenon, we have organized the discussion as follows:

- i. First, we investigate the dynamics of how a macroscale vortex is advected to the porous/fluid interface and whether the solid obstacles of the porous matrix break down the macroscale vortex to microscale size. We will address the question of macroscale vortex survival in a porous medium and the existence of an entrance length for vortex dissipation and establish a baseline of the flow behavior.
- ii. Next, we investigate the effect of porosity on the macroscale vortex transport into the porous layer, specifically targeting porous media with higher porosities (0.8-0.95) to study the boundary cases where macroscale vortices are most likely to persist.
- iii. Finally, we analyze the transport of turbulence kinetic energy inside the porous medium by comparing regions with and without macroscale vortex impingement to highlight the interfacial fluid mechanics.

3.1 Characterization of macroscale vortex impingement on a microscale porous layer

Macroscale vortical structures are introduced onto porous media by upstream turbulence generation by both active mechanisms like pumping and fan-assisted convector or passive mechanisms like bluff bodies or wind gusts. This production of macroscale vortices introduces large scale separation of vortical structures with the porous medium, which leads to multiscale interaction at the porous/fluid interface. To study this phenomenon, we simulated 2D turbulent flow at a pore-scale Reynolds number of 1,000 (see section 2) around a macroscale bluff body with a porous layer of porosity 0.8 situated downstream of it. Under this geometric configuration, large vortices are generated behind the bluff body that are turbulent in nature (Reynolds number for bluff body = 10,000) and their length scale is similar to the size of the bluff body – creating an order of magnitude scale separation between the macroscale vortex and the microscale pores. These macroscale vortices are advected downstream by the flow and impinge on the porous matrix without any significant diminishment of its length scale (Figure 2a).

While these macroscale vortical structures persist upstream of the porous layer, we observed virtually no macroscale structures either within or downstream of the porous layer. Further examination of the flow distribution within the porous layer confirmed that the macroscale vortex is abruptly diminished at the porous/fluid interface indicating geometric confinement due to enhanced local shear near the surfaces of the solid obstacles that comprise the porous matrix. Within the porous layer, the turbulent length scale is therefore confined to the microscale level as evidenced by the microscale vortices that are formed behind the individual solid obstacles of the porous matrix (Figure 2c). These microscale vortices represent the starting point of turbulence production within the porous layer, which typically occurs when the vortex filament produced at the time of microscale vortex generation perturbs the bulk fluid flow leading to vortex stretching, hairpin vortex formation, and eventually, the turbulence energy cascade within the pores as

found by (Srikanth *et al.* 2021). Additionally, consistent with (Srikanth & Kuznetsov 2025) and (Agnaou *et al.* 2016), we observed the formation of secondary oscillatory instability of the flow streamlines deep inside the porous layer, which is a characteristic of fully developed turbulent flow at these porosities.

At the exit of the porous layer, jets of turbulent flow emerge from the individual pores and interact in the clear-fluid region to form vortical structures. However, despite the macroscale size of these downstream vortical structures, they bear no resemblance to the macroscale vortices that were initially produced by the bluff body. Taken together, the streamline plots visualize a clear sequence: macroscale vortices formed upstream of the porous matrix collapse to pore-scale motions inside, then re-expand into larger-scale structures behind the porous layer.

To quantitatively evaluate the length scale of the coherent structures in the model, we calculated the two-point velocity fluctuation correlation function upstream of the porous layer, at the porous/fluid interface, and at the center of the porous layer (Figure 2b). The model predicted that, while the width of the correlation at and upstream of the porous/fluid interface is of macroscale size, the width of the individual peaks of correlation function at the center of the porous layer is of microscale size. This confirmed that the decay of the correlation functions upstream of the porous layer are identical, indicating that the dominant vortex length scale at these locations is set by the bluff body size. Whereas the rapid decay in the correlation function within the porous layer suggests pore-scale suppression where the length scales within the porous matrix are significantly smaller than those in the surrounding clear-fluid region.

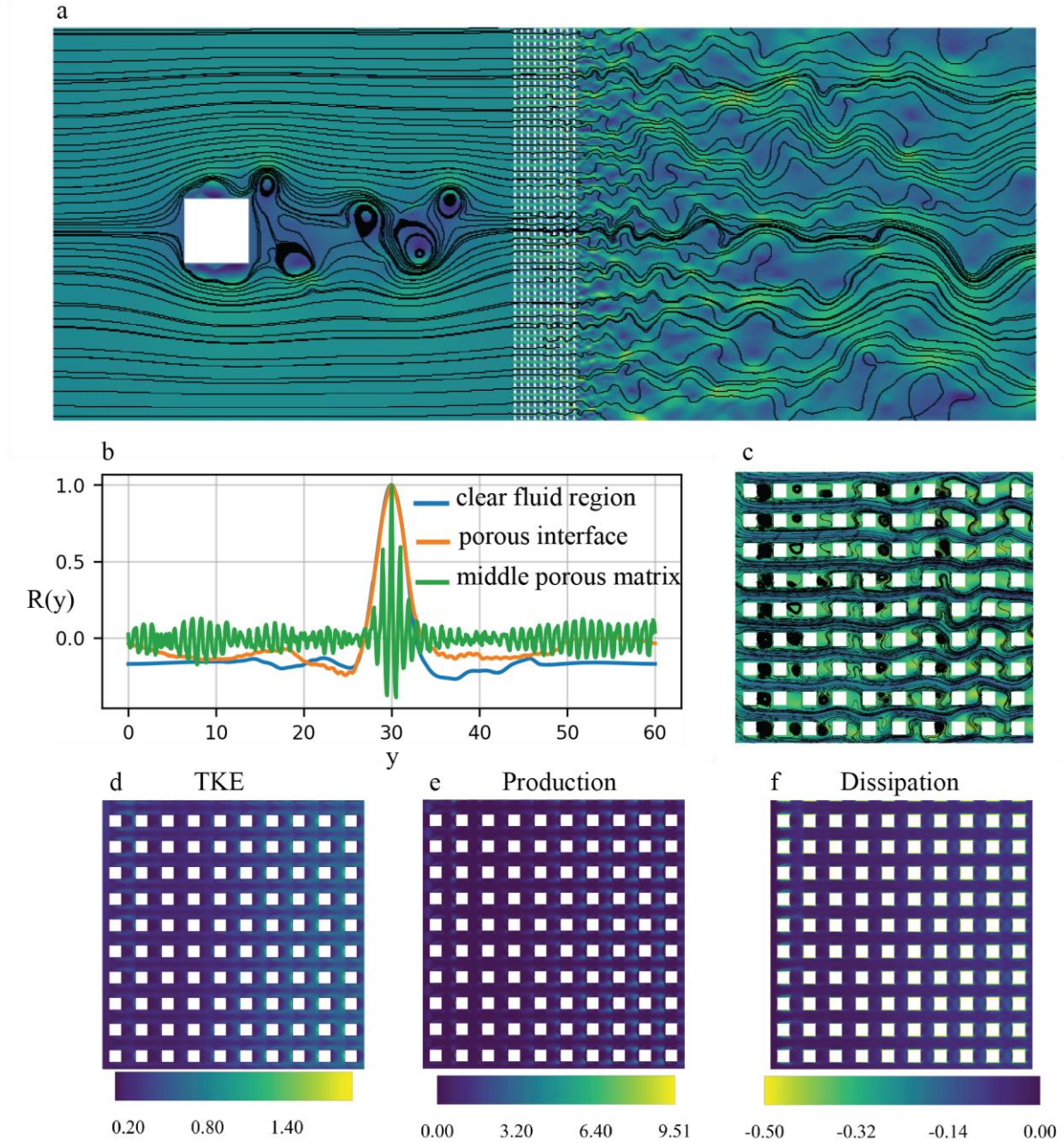


Figure 2: Macroscale vortices transition to microscale size when they impinge on a porous layer (porosity = 0.80): (a) Instantaneous x -velocity contours and streamlines show macroscale vortex production by the bluff body and its transport to the porous layer, where the macroscale structures disappear at the porous/fluid interface. (b) Two-point correlation function of velocity fluctuation reveals the diminished correlation value at the center of the porous layer (green) when compared to the upstream (blue) and interface (orange) locations signifying vortex breakdown. (c) A zoomed view of the porous layer at the interface confirms only microscale vortex persistence in the porous layer. The distributions of (d) turbulence kinetic energy, (e) production, and (f) dissipation which illustrate the budget of transport terms and reveal the sequence of microscale transport within the porous layer.

Intriguingly, the correlation function at the center of the porous layer revealed a large-scale

correlation superimposed on the individual peaks that denote micro-scale level correlation. To understand this behavior, we analyzed the budget of turbulence kinetic energy transport by interpreting the results within the Kraichnan-Leith-Batchelor framework of 2D turbulence, as detailed in section 2. The distribution of TKE within the porous layer reveals that initially elevated peak value of TKE at the porous/fluid interface drops twofold within the first three columns of solid obstacles leading to weak fluctuations in the flow (Figure 2d). This is caused by significant negative production in the stagnant face of the porous/fluid interface – a characteristic of porous flows (He *et al.* 2019)– and high dissipation rate of the flow at the interface that is caused by strong shear at the solid obstacle surface (Figure 2f). As a result of this weak turbulence near the center of the porous layer, correlations persist between the jetting flow patterns between the solid obstacles of the porous matrix. These correlations do not represent a single macroscale vortex surviving inside the porous layer, but rather the effect of the undamped momentum deficit introduced by the macroscale vortex wake.

3.2 *The effect of porosity on macroscale vortex destruction at the porous/fluid interface*

Our simulation results demonstrated that macroscale vortices are rapidly broken down upon impingement at a porous layer with constrained porosity, creating a jump discontinuity in the length scale of coherent motions at the interface. For a most robust confirmation of this phenomenon, we investigated whether this behavior is consistent across different porosities by focusing on high porosity media, which may be less effective at diminishing turbulent motions due to the smaller surface area to pore volume ratio. We simulated 2D turbulent flow by following the same procedure as in the previous section and varied the porosity (0.8, 0.85, 0.9, 0.95) such that the separation distance between the solid obstacles of the porous matrix is held constant, ensuring a constant scale separation between the bluff body and the pore scale. Similar to the porosity of 0.8, the macroscale vortex is completely and abruptly broken down at the porous/fluid interface at all tested values of porosity (Figure 3). While the macroscale vortical motion very evidently becomes confined to the pore-scale, the streamlined flow patterns within the porous layer observed at low porosity become more irregular as the porosity is increased. The microscale flow at high porosity is less constrained by the strong shear layers generated between the solid obstacles. When combined with the formation of shedding microscale vortices, this leads to strong instabilities in the microscale flow. However, this observation is also independent of the impinging macroscale vortex since these instabilities are observed in both the impingement and non-impingement regions of the porous layer, as discussed later.

The primary influence of the impinging macroscale vortex on the microscale flow in the porous layer becomes evident at high porosity at the porous/fluid interface, where the localized macroscale flow direction is not aligned with the direction of free-stream velocity (the x -direction). This results in macroscale streamline tortuosity at the interface with a non-trivial penetration depth between 3-5 pore sizes depending on the porosity. This behavior is more readily visualized when observing macroscale vortex collapse as they impinge upon the porous matrix (Figure 4). As the macroscale vortex approaches the porous/fluid interface, it introduces a region of low pressure and high vorticity near the porous obstacles that generates macroscale flow and influences the microscale vortex formation within the pores. This is characterized by strong streamline curvature and asymmetrical flow patterns at the microscale level around the solid obstacles of the porous matrix. The intense shear generated by this flow is associated with enhanced turbulent production and dissipation rate, which locally removes turbulent kinetic energy of the flow and contributes to the breakdown of the macroscale vortex. In contrast, regions that are not exposed to vortex impingement exhibit a more regular pattern: low-velocity wakes form directly behind the obstacles, and

high-velocity jets occupy the vertical gaps between unit cells. This organization inhibits vertical transport between rows of solid obstacles and promotes more symmetrical flow patterns primarily oriented in the free-stream direction. Deep inside the porous layer, the flow patterns become qualitatively indistinguishable between the impingement and non-impingement regions with the exception of the momentum deficit caused in the flow velocity behind the macroscale bluff body.

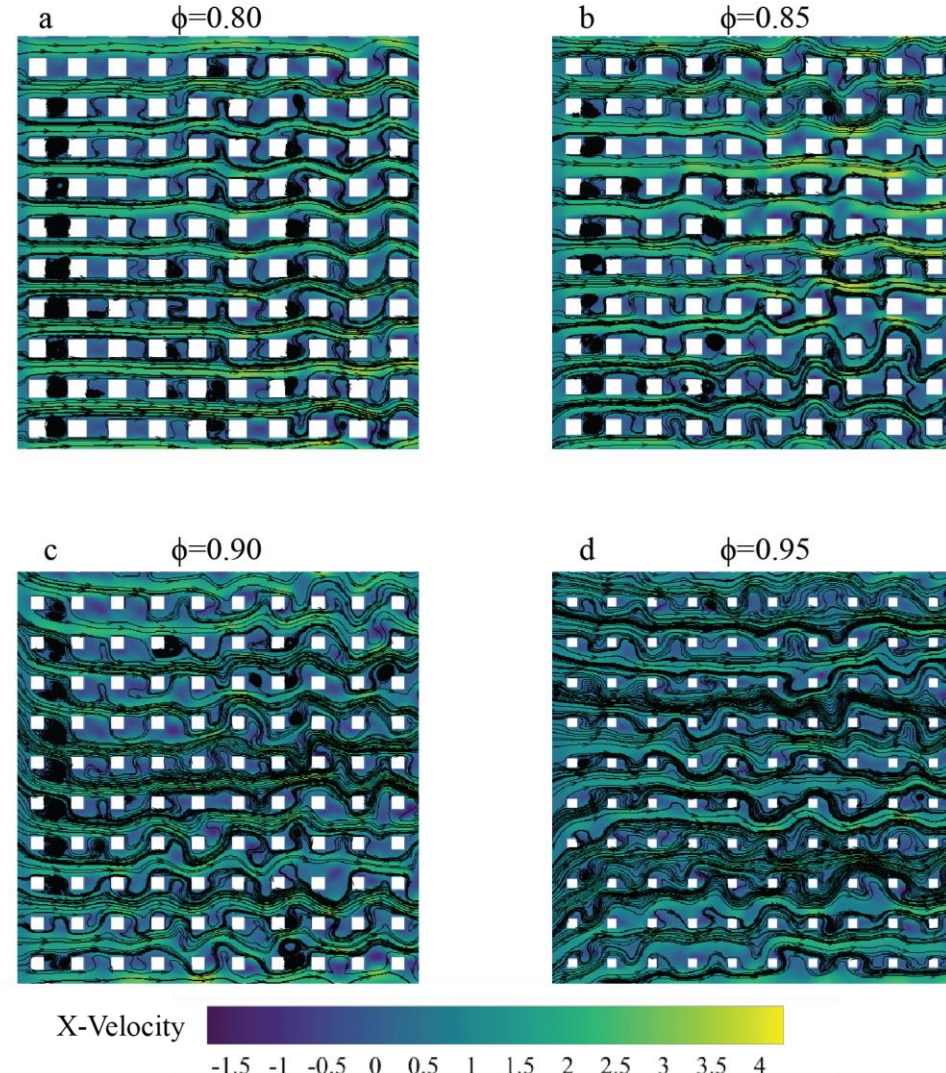


Figure 3: Contours of x -velocity and streamlines at an instant in time for porosities (a) 0.80, (b) 0.85, (c) 0.90, and (d) 0.95. Vortex size is constrained by the distance between porous obstacles and cannot exist on a macroscale due to the presence of the porous obstacles.

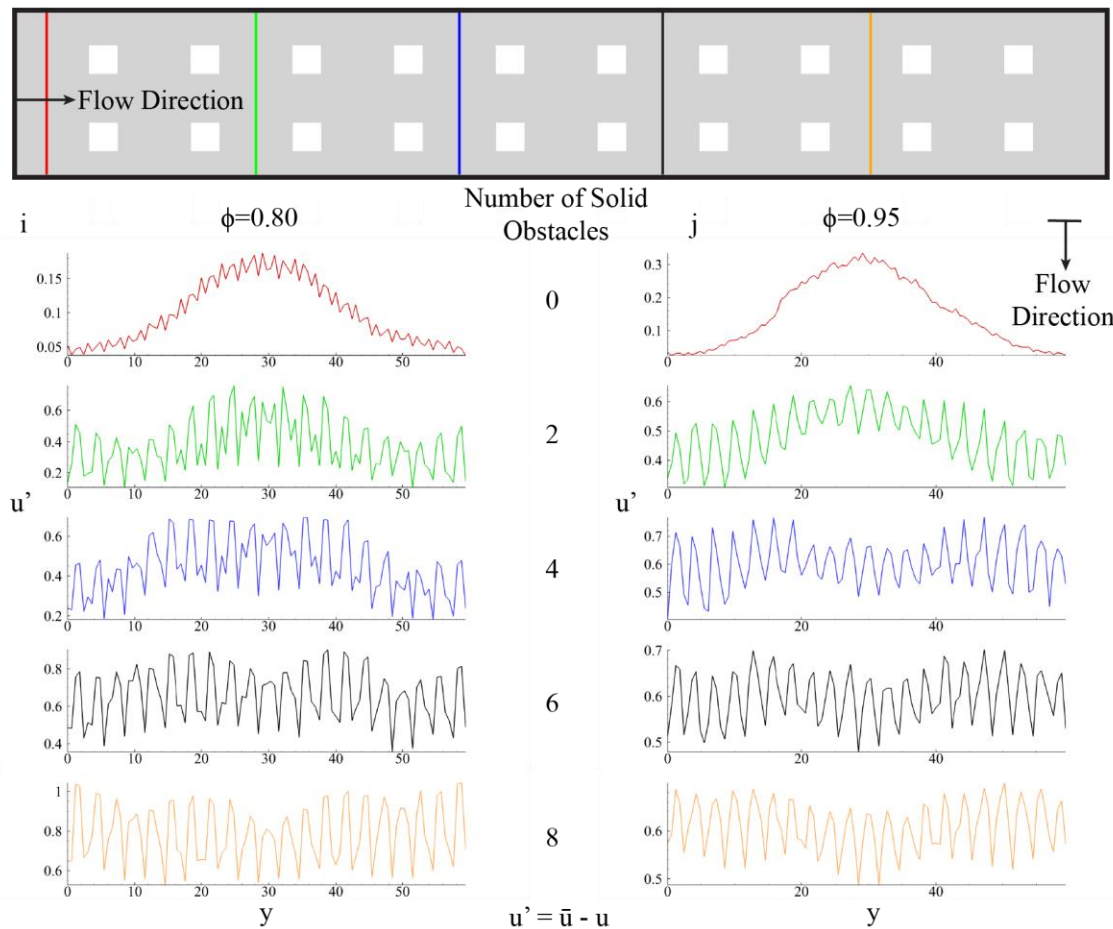
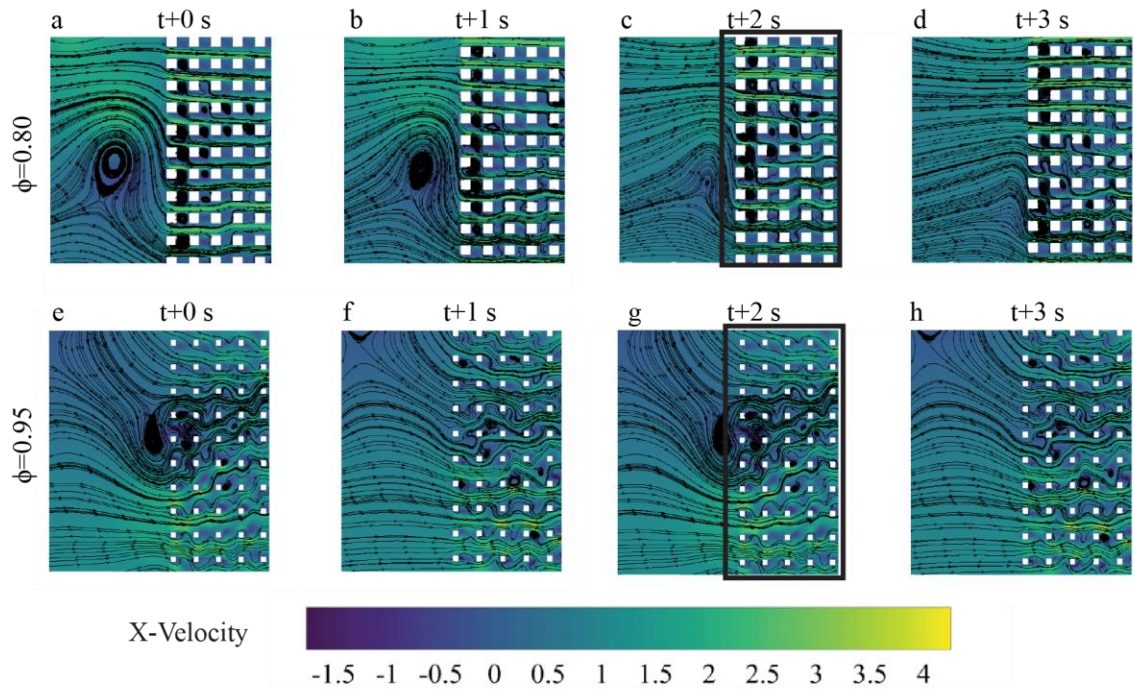
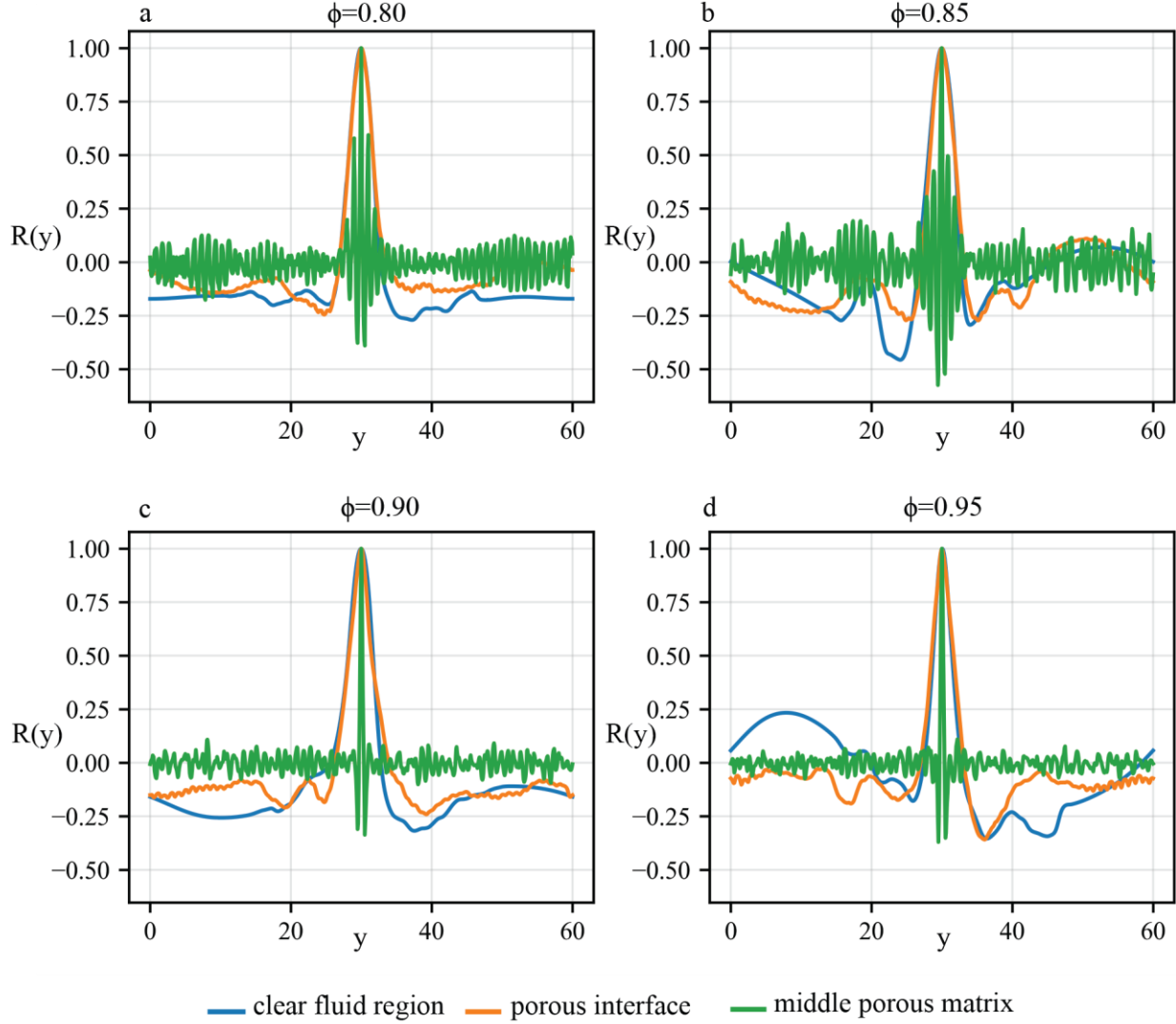


Figure 4: Contours of x -velocity and streamlines as a function of time for porosities $\phi = 0.80$ (a-d) and $\phi = 0.95$ (e-h) after the simulation has achieved a statistically steady state. The vortex is clearly formed in (a, e) and moves toward the porous matrix in (b, f) where streamlines begin to bend and velocity gradients increase. It starts to dissipate as it nears the porous matrix (c, g) and in (d, h), the macroscale turbulent structure has lost its coherence. (i) and (j) show the fluctuating components of velocity as the macroscale vortex moves further into the porous matrix. In both cases, it clearly dissipates at around 2-4 obstacles.

Since the macroscale vortex influenced microscale flow patterns within the pores at high porosity, we asked whether this constituted a macroscale coherent structure within the porous layer. Therefore, we calculated the two-point correlation function of the velocity fluctuations at the same locations as previously: upstream, interface, and the center of the porous layer (Figure 5a). The correlation functions upstream and at the porous/fluid interface at different porosities confirmed nearly identical coherent length scales of the macroscale vortex prior to impingement. Interestingly, within the porous layer, the correlation function exhibited a tighter peak at higher porosities compared to the lower porosities, signaling a complete destruction of any macroscale coherence of the flow inside the porous layer despite the deeper penetrating influence of the macroscale vortex. To understand this counterintuitive result – deeper propagation of macroscale vortical motion did not result in a wider correlation function, we examined the volume-averaged turbulence kinetic energy distribution inside the porous layer (Figure 6). At the porous/fluid interface, a positive correlation between the volume-averaged TKE and porosity is observed. This correlation is reversed at the exit of the porous layer as the flow develops and more microscale TKE is produced by the porous matrix. Note that these same trends are observed in regions where no vortex impingement occurs suggesting that this is an intrinsic property of the porous layer independent of macroscale influence. However, this enhanced turbulence intensity upon impingement at high porosity, driven by the less constrained pore space, enables the pore-scale flow to perturb the induced macroscale patterns and destroy its coherence. This provides a physical explanation for this paradoxical behavior of the correlation function at high porosities.



Integral Length Scale (m)				
Porosity	0.80	0.85	0.90	0.95
Porous Interface	1.54	1.68	1.66	1.66
Middle Porous Matrix	0.10	0.17	0.21	0.24
Middle Porous Matrix Non-Impingement Region	0.10	0.16	0.22	0.24

Figure 5: Correlation functions for porosities (a) 0.80, (b) 0.85, (c) 0.90, and (d) 0.95 for 3 regions of interest within the fluid domain and their integral length scales. The first (blue) is the clear fluid region directly downstream of the large solid obstacle where macroscale turbulence is unconstrained. Turbulent structures travel to the clear fluid/porous interface (orange) after the clear fluid region. At this location, the macroscale eddies continue to exist because they are not yet confined by the porous matrix. Finally, midway through the porous matrix (green), the eddy size is significantly diminished due to the pore constraints. The

integral length scale in the impingement and impingement free regions are similar, indicating that the macroscale vortices are confined to the porous length scale.

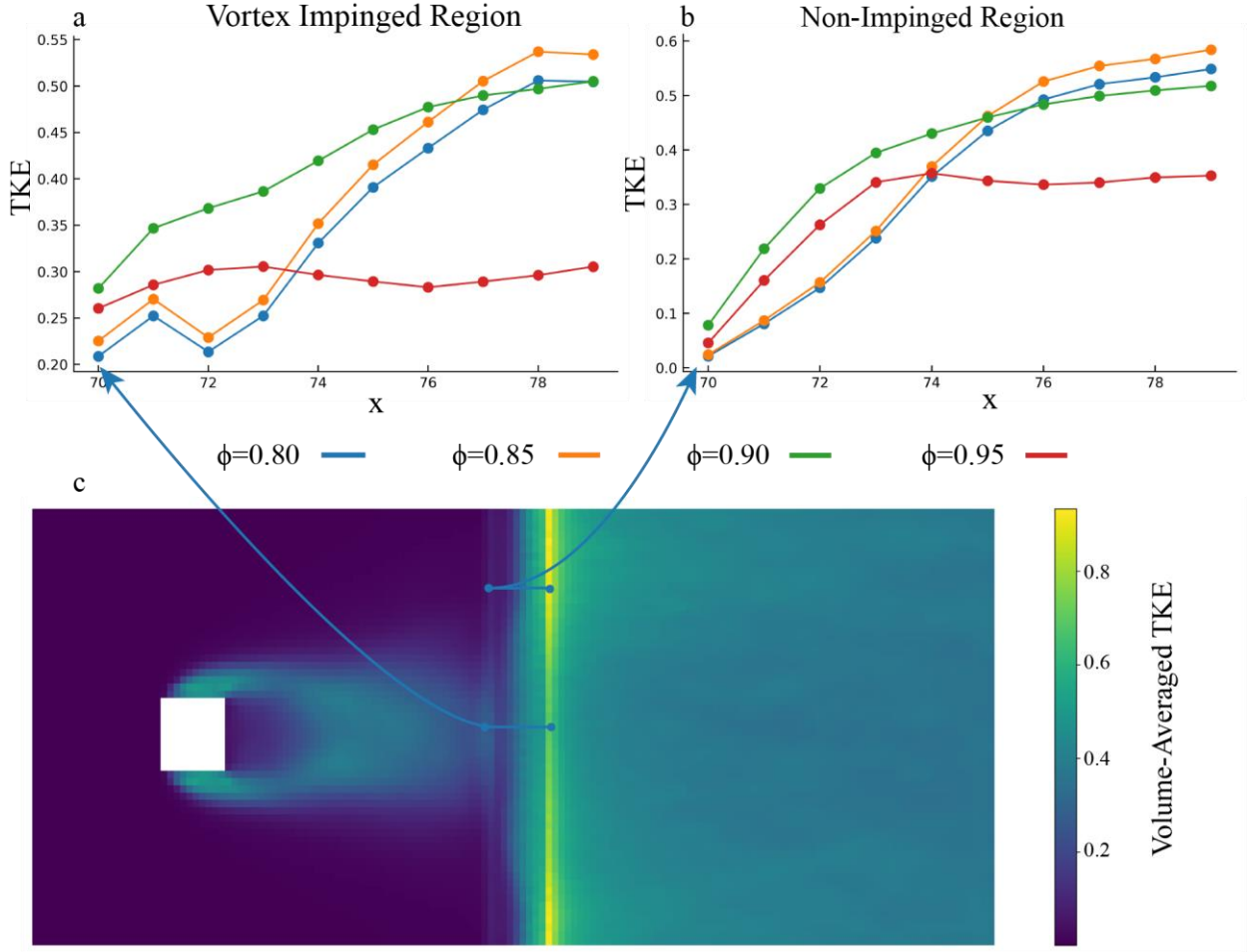


Figure 6: TKE vs distance into the porous matrix for different porosities in (a) the region subjected to vortex impingement, at (b) the region free from the impact of vortex impingement, and (c), the volume-averaged TKE for the entire flow domain for a porosity of 0.80.

3.3 The effect of macroscale vortex impingement on TKE transport inside the pores

Based on our analysis, macroscale vortex impingement dramatically influences the turbulence kinetic energy distribution inside the porous layer, especially at the porous/fluid interface where the impingement occurs. We developed a more thorough phenomenological understanding of these behaviors by calculating a budget of the TKE transport within the pores. We accomplished this by calculating the terms of the macroscopic TKE equation (given in Appendix A), which relates the temporal evolution and advection of the volume-averaged TKE to five principal terms: production, pressure diffusion, viscous diffusion, turbulent transport, and viscous dissipation. The spatial evolution of TKE within the porous layer is governed by a competitive balance between inherited upstream fluctuations and locally generated pore-scale shear. By examining the TKE budget across varying porosities and impingement conditions, specifically comparing regions of direct vortex impingement with non-impinged and no-bluff-body control cases, we delineate the mechanisms through which the porous matrix modifies the flow physics.

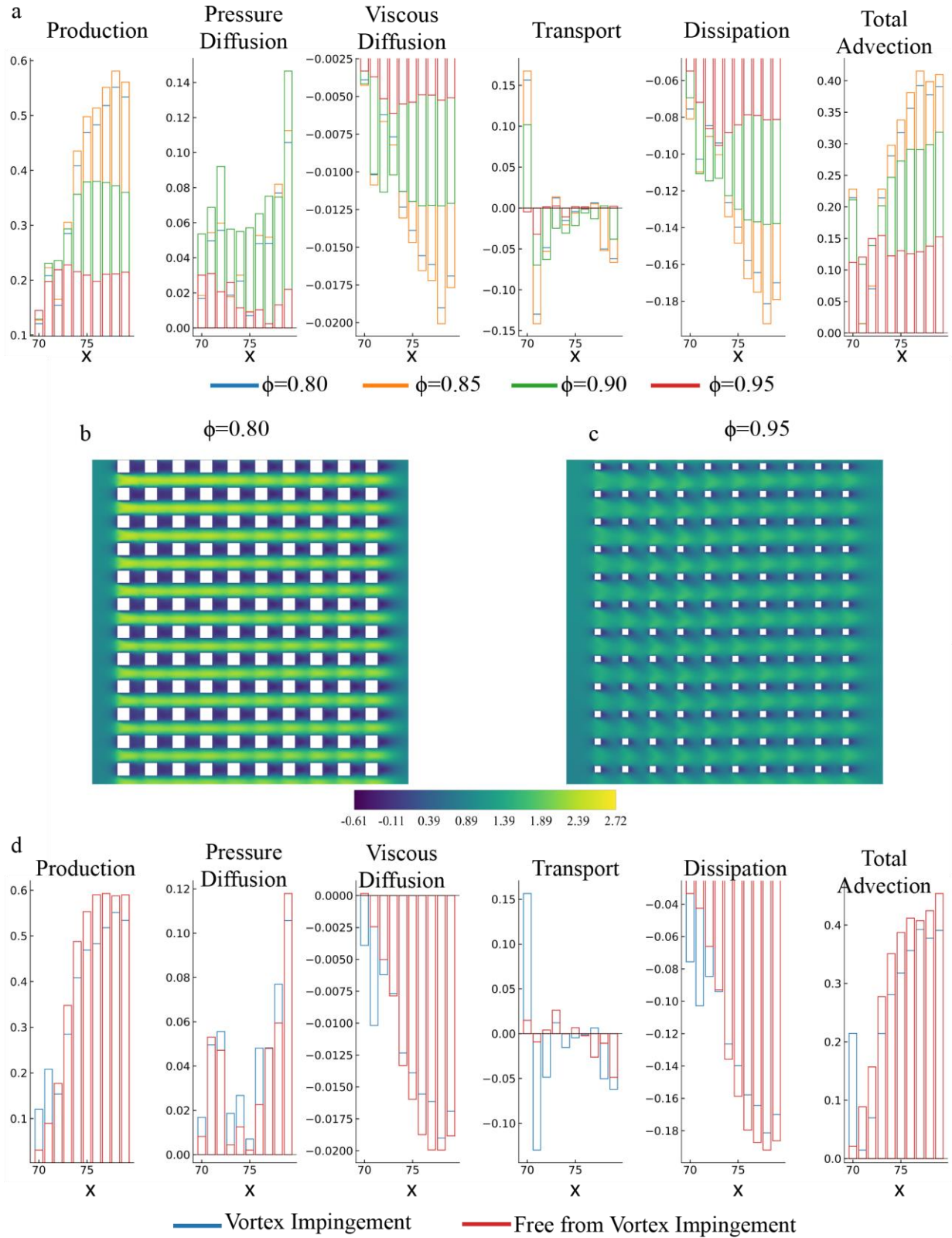


Figure 7: (a) Terms in the TKE Transport Equation in the vortex impinged region for different porosities. From left to right: Turbulent Production, Pressure Diffusion, Viscous Diffusion, Turbulent Transport, Dissipation, and Total Advection which is the sum of the preceding terms. (b)/(c) Mean velocity profiles for a porosity of 0.80 and 0.95. The mean velocities increase with distance from the streamwise midplane resulting in higher velocity gradients (these differences are subtle but noticeable). (d) Terms in the TKE transport equation as a function of distance into the porous matrix in the vortex impinged region (blue) and the region free from vortex impingement (red) for $\phi = 0.85$.

The spatial evolution of the turbulent kinetic energy (TKE) budget reveals a distinct two-stage process characterized by the structural filtering of upstream fluctuations and the subsequent emergence of pore-scale production. At the porous interface, the initial TKE distribution is bifurcated. In the interface regions subjected to macroscale vortex impingement, the budget is dominated by turbulent transport, which is the divergence of the triple velocity correlation, and conveys large-scale fluctuations from the upstream wake being injected into the porous layer. This is evidenced by a sharp positive peak in the transport term at the porous/fluid interface (Figure 7a), signifying a net influx of energy. Conversely, in the non-impinged regions and the no-bluff-body control case, the inflow remains only weakly turbulent or laminar (TKE < 0.05), and the initial transport of TKE is negligible (Figure 7d). This disparity establishes a fundamental trade-off. While the impinged regions benefit from an initial injection of turbulent energy, the associated wake introduces a momentum deficit that limits the magnitude of the mean velocity gradients. In the non-impinged control regions, the higher momentum of the unobstructed flow preserves sharper gradients, providing a higher potential for shear production once pore-scale instabilities are triggered.

This supplied TKE in the impinged regions is rapidly attenuated, as indicated by an immediate negative dip in the transport term following the first obstacle row. Physically, this transition represents a structural bottleneck where the porous geometry shatters the incoming macroscale vortices, exporting or decorrelating the inherited fluctuations faster than local mechanisms can sustain them. This budgetary redistribution causes TKE levels to drop after the inlet, especially at low porosity where the flow is constrained (Figure 6a). Within this region, the transport term remains negligible, indicating that the flow has been stripped of its injected turbulent structures. Therefore, deep inside the porous layer ($\sim 3-5$ obstacle layers), turbulence transport transitions from the external influence of the macroscale vortex to the internal generation of microscale vortices in the porous matrix.

The TKE budget reflects a localized equilibrium between production and viscous dissipation, presenting the most dominant terms of TKE transport followed by pressure diffusion. The production of TKE depends on two components: (i) mean velocity gradients, which provide the mean shear, and (ii) turbulent fluctuations, quantified by the Reynolds stresses, on which the mean shear does work. Large mean velocity gradients stretch and tilt the turbulent eddies, thereby increasing the Reynolds stresses and amplifying production, which transfers energy from the mean flow into TKE. Pressure diffusion of TKE becomes significant due to the constant interaction of the flow with the solid obstacles of the porous matrix creating oscillatory regions of stagnation pressure on the solid obstacle surface. However, because production is the predominant term in the TKE transport equation, the magnitudes of the mean velocity gradients and Reynolds stresses are strong candidates for explaining how TKE varies with porosity. The magnitude of production is constrained by the geometric confinement of the pores; as porosity decreases, the fluid is forced through narrower interstitial gaps, intensifying the mean velocity gradients between the high-speed pore centerlines and the no-slip obstacle walls. This intensification amplifies the shear production term, which acts as the primary driver of TKE growth.

One notable exception occurs for $\phi = 0.85$, where the production slightly exceeds that of the $\phi = 0.80$ case; this behavior is due to greater scaling of the mean velocity gradients by larger Reynolds stresses. Dissipation is also enhanced in regions of large velocity gradients. Physically, sharper velocity gradients mean that neighboring fluid layers slide and stretch past one another more strongly, so viscosity does more work against the fluctuating motion and converts turbulent kinetic energy into internal energy. Mathematically, this is reflected in the dissipation term in Appendix A, which is proportional to the sum of the squares of the fluctuating velocity gradients. As mean shear strengthens, the resulting turbulent fluctuations develop steeper gradients at smaller scales, leading to higher dissipation. As a result, production and dissipation tend to scale with one another and exhibit similar spatial trends: locations with large production magnitudes also show large dissipation magnitudes, and vice versa.

In lower-porosity cases, this stronger production allows the TKE to reach a larger peak farther downstream into the porous matrix than in higher-porosity cases (Figure 6a/Figure 6b). For higher porosities, production and dissipation attain their maximum values near the entrance of the porous matrix and then decay gradually and grow again (Figure 7a). The streamlines are less constrained than in lower-porosity cases and can traverse multiple rows of obstacles; as a result, the mean velocity gradients are weaker, and the production peak is smaller, which limits the peak TKE. Beyond the observed peak, we expect production and dissipation in the low-porosity cases to exhibit a similar qualitative sequence to that in the highest-porosity case – an initial decay followed by gradual growth – but with more pronounced variations.

A notable paradox emerges during this secondary growth phase: despite the lack of initial upstream turbulence, the non-impinged regions often achieve higher peak TKE levels deep within the matrix than the impinged regions (compare Figure 6a and Figure 6b; Figure 7d). This occurs because the sustained, higher mean velocity gradients in the non-impinged flow drive more vigorous shear production than the "pre-disturbed" wake flow, where the momentum deficit suppresses the production term (Figure 7d). The downstream growth of TKE is eventually arrested by a mechanism of wake-channel blending, wherein microscale eddies formed in the obstacle wakes increasingly oscillate into the adjacent high-speed interstitial channels. In the absence of this exchange, one would expect a local positive feedback loop where increasing production raises TKE, which in turn amplifies the Reynolds stresses to further drive production. However, this repeated transverse momentum exchange causes the wake and channel regions to bleed into one another: high-speed fluid loses momentum to the eddies, and low-speed wake fluid is re-energized. In the mean field, this appears as an acceleration–deceleration pattern where the flow is alternately throttled between obstacles and diffused into the wakes, effectively thinning the velocity and TKE gradients at the wake-channel interface. This reduction in local shear limits further growth of the production term and sets a finite peak for the TKE. Notably, the region where TKE saturates emerges further into the porous matrix for low-porosity cases but is pushed closer to the inlet as porosity increases, as the wake eddies are less confined and can more readily perturb the free-stream momentum. The convergence of the TKE profiles for the impinged, non-impinged, and no-bluff-body cases toward a nearly identical state deep within the matrix confirms that the porous architecture acts as a definitive spatial filter. Ultimately, the internal geometry erases the upstream history and forces the turbulence into a locally determined equilibrium governed solely by the pore-scale Reynolds number and geometric constraints.

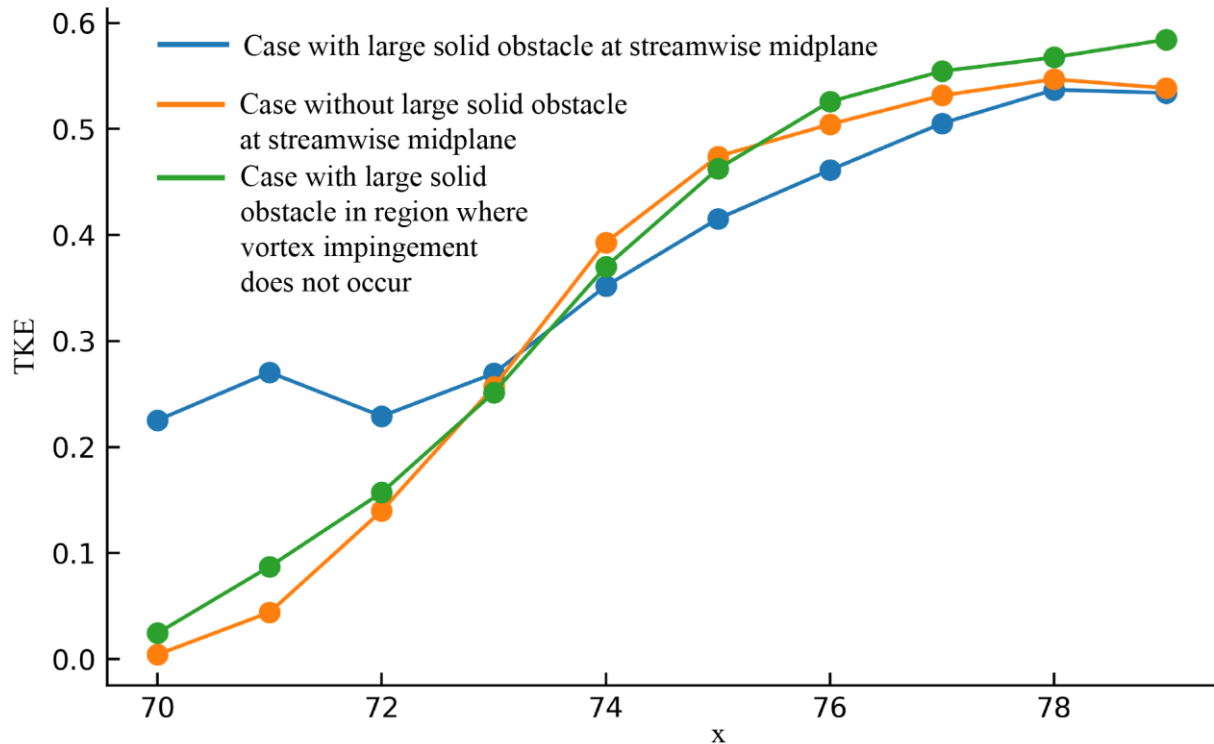


Figure 8: TKE comparison for a porosity of 0.85 with and without a large solid obstacle upstream of the porous matrix. The blue line is across the streamwise midplane for the case with a large solid obstacle where vortex impingement occurs on the porous matrix. The orange line is at the same location but for the case where no upstream vortices are induced and no vortex impingement occurs. The green is for the case with the large solid obstacle but at a location where vortex impingement does not occur.

4 Conclusions

The resolution of how macroscale turbulent structures penetrate and evolve within porous media remains a critical challenge in fluid mechanics. In this paper, we investigated the impact of macroscale vortex impingement on the transport of turbulence kinetic energy within a porous matrix considering different porosities ($\phi=0.80, 0.85, 0.90, 0.95$). We found that the macroscale vortices are broken down upon impingement and this is simultaneously accompanied by microscale vortex production inside the porous matrix.

This abrupt scale collapse has direct consequences for the turbulent kinetic energy budget within the porous layer. Analysis of the volume-averaged TKE transport equation revealed that, although macroscale vortex impingement introduces a localized influx of turbulent energy at the porous/fluid interface, this supplied TKE is rapidly redistributed and dissipated as the flow reorganizes to satisfy pore-scale constraints. Deeper within the matrix, turbulence is sustained primarily by local shear production associated with microscale velocity gradients imposed by the solid obstacles, rather than by direct transport of macroscale structures. As a result, the internal turbulence becomes increasingly independent of upstream forcing, approaching a locally determined equilibrium governed by the pore-scale Reynolds number and geometry.

Porosity was found to play a dual role by simultaneously controlling geometric confinement and effective Reynolds number within the pores. Decreasing porosity intensified mean velocity gradients and enhanced both production and dissipation of TKE, leading to an overall inverse relationship between volume-averaged TKE and porosity. An intermediate porosity ($\phi \approx 0.85$) produced the highest turbulence levels due to a favorable balance between strong shear and sufficient pore connectivity. In contrast, higher-porosity matrices permitted deeper penetration of impingement-induced disturbances but exhibited weaker shear production, limiting the growth of TKE. Importantly, regions subjected to vortex impingement consistently displayed lower peak TKE deep within the matrix than non-impinged regions, owing to the momentum deficit inherited from the upstream wake, which suppresses shear-driven production.

Taken together, these results provide strong support for the pore-scale prevalence of turbulence even in the presence of externally forced macroscale vortices. The porous matrix acts as a robust geometric filter that erases the upstream turbulent history and enforces a rapid transition to pore-scale-dominated dynamics. These findings have implications for the design of porous materials used in flow control, filtration, heat transfer, and drag-modification applications, where external turbulence is unavoidable. More broadly, they demonstrate that the interaction between external coherent structures and porous media must be understood through the redistribution of turbulent kinetic energy across scales, rather than through the survival of macroscale vortices themselves.

Future results should explore the effects of varying obstacle shapes and scale separation on vortex behavior and TKE transport and cascade, as well as the impact of random solid-obstacle arrangements. Assessing how stochasticity of the porous medium alters penetration depth, interfacial production, turbulence and pressure diffusion, and dissipation across successive pore layers will clarify the role of geometric variability on turbulence transport in porous media. It may also explore the impact of the length of the porous matrix on the TKE answering questions such as: will the TKE in the porous region subject to vortex impingement approach that of the region without impingement at large enough distances into the porous matrix?

Appendix A: Governing Equations of the DNS Model

In this study, we used a Direct Numerical Simulation (DNS) in Ansys Fluent 21.2 which solves the incompressible Navier-Stokes equations. The results are reported in SI units, and the equations are identified below.

Continuity Equation:

$$\frac{\partial u_i}{\partial x_i} = 0 \quad (8)$$

Momentum
(Navier-Stokes)
Equations:

$$\frac{\partial u_i}{\partial t} + u_j \frac{\partial u_i}{\partial x_j} = -\frac{1}{\rho} \frac{\partial p}{\partial x_i} + \nu \frac{\partial^2 u_i}{\partial x_j^2} + f_{b,i} \quad (9)$$

Appendix B: TKE Transport Equation

The volume-averaged TKE transport equation is based on Section 4.2 in (de Lemos 2012) .

The transport equation for TKE is:

$$\begin{aligned} \frac{\partial k}{\partial t} + \bar{u}_j \frac{\partial k}{\partial x_j} = & -\frac{1}{\rho_0} \frac{\partial}{\partial x_j} \bar{u}'_i \bar{p}_i' - \frac{1}{2} \frac{\partial}{\partial x_i} \bar{u}'_j \bar{u}'_j \bar{u}'_i + \nu \frac{\partial^2 k}{\partial x_j^2} - \bar{u}'_i \bar{u}'_j \frac{\partial \bar{u}_i}{\partial x_j} \\ & - \nu \frac{\partial \bar{u}_i}{\partial x_j} \frac{\partial \bar{u}_i}{\partial x_j} - \frac{g}{\rho_0} \bar{u}'_i \bar{p}_i' \delta_{i3} \end{aligned} \quad (10)$$

where TKE is defined as:

$$k = \frac{1}{2} \bar{u}'_i \bar{u}'_i \quad (11)$$

Each term may then be expanded so that it is no longer dependent on fluctuating velocity components. Because the simulations are statistically stationary, the volume-averaged temporal derivative vanishes, leaving only the spatial derivatives.

$$\frac{\partial k}{\partial t} + \bar{u}_j \frac{\partial k}{\partial x_j} = -\frac{1}{\rho_0} \frac{\partial}{\partial x_j} \bar{u}'_i \bar{p}_i' - \frac{1}{2} \frac{\partial}{\partial x_i} \bar{u}'_j \bar{u}'_j \bar{u}'_i + \nu \frac{\partial^2 k}{\partial x_j^2} - \bar{u}'_i \bar{u}'_j \frac{\partial \bar{u}_i}{\partial x_j} - \nu \frac{\partial \bar{u}_i}{\partial x_j} \frac{\partial \bar{u}_i}{\partial x_j} - \frac{g}{\rho_0} \bar{u}'_i \bar{p}_i' \delta_{i3}$$

Production Term

$$P = - \left[(\bar{u}^2 - \bar{u}^2) \frac{\partial \bar{u}}{\partial x} + (\bar{u}\bar{v} - \bar{u}\bar{v}) \frac{\partial \bar{u}}{\partial y} + (\bar{v}\bar{u} - \bar{v}\bar{u}) \frac{\partial \bar{v}}{\partial x} + (\bar{v}^2 - \bar{v}^2) \frac{\partial \bar{v}}{\partial y} \right] \quad (12)$$

Pressure Diffusion Term

$$D_p = -\frac{1}{\rho} \left[\frac{\partial}{\partial x} (\bar{u}\bar{p} - \bar{u}\bar{p}) + \frac{\partial}{\partial y} (\bar{v}\bar{p} - \bar{v}\bar{p}) \right] \quad (13)$$

Turbulent Transport Term

$$\begin{aligned} T = & -\frac{1}{2} \left[\frac{\partial}{\partial x} \left(\bar{u}^3 + \bar{v}^2 \bar{u} - (\bar{u}^2 \bar{v} + \bar{v}^2 \bar{u}) - 2(\bar{u}\bar{u}^2 + \bar{v}\bar{v}\bar{u}) + 2(\bar{u}^3 + \bar{v}^2 \bar{u}) \right) \right. \\ & + \frac{\partial}{\partial y} \left(\bar{v}^3 + \bar{u}^2 \bar{v} - (\bar{u}^2 \bar{u} + \bar{v}^2 \bar{v}) - 2(\bar{v}\bar{v}^2 + \bar{u}\bar{u}\bar{v}) \right. \\ & \left. \left. + 2(\bar{v}^3 + \bar{u}^2 \bar{v}) \right) \right] \end{aligned} \quad (14)$$

Viscous Diffusion Term

$$D_v = \frac{\nu}{2} \left[\frac{\partial^2}{\partial x^2} \left((\bar{u}^2 - \bar{u}^2) + (\bar{v}^2 - \bar{v}^2) \right) + \frac{\partial^2}{\partial y^2} \left((\bar{u}^2 - \bar{u}^2) + (\bar{v}^2 - \bar{v}^2) \right) \right] \quad (15)$$

Dissipation Term

$$\varepsilon = \nu \left[\overline{\left(\frac{\partial u}{\partial x} \right)^2} + \overline{\left(\frac{\partial u}{\partial y} \right)^2} + \overline{\left(\frac{\partial v}{\partial x} \right)^2} + \overline{\left(\frac{\partial v}{\partial y} \right)^2} - \left[\overline{\left(\frac{\partial \bar{u}}{\partial x} \right)^2} + \overline{\left(\frac{\partial \bar{u}}{\partial y} \right)^2} + \overline{\left(\frac{\partial \bar{v}}{\partial x} \right)^2} + \overline{\left(\frac{\partial \bar{v}}{\partial y} \right)^2} \right] \right] \quad (16)$$

Appendix C: Adequacy of the Grid Resolution

In the present study, our goal is to investigate the macroscale turbulent vortex structures as well as the microscale structures that exist in the porous matrix. The flow properties associated with these structures are utilized to generate the governing terms in the TKE transport equations, the TKE, and characterizations of the flow such as the correlation functions. In this section, we show that the grid resolution used is adequate to achieve these objectives. We consider the bounding porosity cases run of 0.80 and 0.95 rather than all 4 cases due to computational constraints as a part of this study. Since the grid size in all cases is the same, the adequacy of the grid resolution for the bounding porosities is assumed to be applicable for the other porosities as well. The Reynolds number at the large solid obstacle is maintained at 1000, and the near wall grid resolution is held constant such that the non-dimensional near wall grid height is less than 1.

$$y^+ = \frac{y \rho u_\tau}{\mu} \quad (17)$$

We tested 3 values of the maximum grid size: at a $\Delta x/s$ of 0.01, 0.015, and 0.02.

Table 1: Percentage change in the total drag coefficient due to grid refinement.

Change in grid resolution	$\Phi = 0.80$	$\Phi = 0.95$
$\Delta x/s = 0.01-0.15$	2.5%	4.6%
$\Delta x/s = 0.01-0.20$	11.0%	11.8%

References

Abderrahaman-Elena, N., & García-Mayoral, R. (2017). Analysis of anisotropically permeable surfaces for turbulent drag reduction. *Physical Review Fluids*, 2(11), 114609.

Agnaou, M., Lasseux, D., & Ahmadi, A. (2016). From steady to unsteady laminar flow in model porous structures: an investigation of the first Hopf bifurcation. *Computers & Fluids*, 136, 67–82.

Mayer, B. (2014). *Investigations of Pressure Loss and Heat Transfer in a Regular Metallic Porous Structure* (PhD Thesis, B. Weigand, adviser), University of Stuttgart.

Blackburn, H. M., & Lopez, J. M. (2003). On three-dimensional quasiperiodic Floquet instabilities of two-dimensional bluff body wakes. *Physics of Fluids*, 15(8), L57–L60.

Chen, J., & Wu, J. (2024). Numerical investigation of vortex-induced vibration of a porous-coated cylinder at subcritical Reynolds number with a combined k- ϵ model for porous medium. *Ocean Engineering*, 304, 117828.

Chen, L., Zhao, Y., Gao, Y., & Weigand, B. (2025). Detailed numerical study on jet impingement heat transfer using porous lattice structures and multi-objective optimization of lattice cells. *Applied Thermal Engineering*, 279, 127705.

Chu, X., Wang, W., Yang, G., Terzis, A., Helmig, R., & Weigand, B. (2021). Transport of Turbulence Across Permeable Interface in a Turbulent Channel Flow: Interface-Resolved Direct Numerical Simulation. *Transport in Porous Media*, 136(1), 165–189.

Chu, X., Weigand, B., & Vaikuntanathan, V. (2018). Flow turbulence topology in regular porous media: From macroscopic to microscopic scale with direct numerical simulation. *Physics of Fluids*, 30(6). doi:10.1063/1.5030651

Chu, X., Yang, G., Pandey, S., & Weigand, B. (2019). Direct numerical simulation of convective heat transfer in porous media. *International Journal of Heat and Mass Transfer*, 133, 11–20.

de Lemos, M. J. S. (2012). *Turbulence in porous media : modeling and applications*, Elsevier.

Gasow, S., Lin, Z., Zhang, H. C., Kuznetsov, A. V., Avila, M., & Jin, Y. (2020). Effects of pore scale on the macroscopic properties of natural convection in porous media. *Journal of Fluid Mechanics*, 891, A25.

Hanspal, N. S., Nassehi, V., & Kulkarni, A. (2013). Three-dimensional finite element modelling of coupled free/porous flows: applications to industrial and environmental flows. *International Journal for Numerical Methods in Fluids*, 71(11), 1382–1421.

Hao, Z., & García-Mayoral, R. (2025). Turbulent flows over porous and rough substrates. *Journal of Fluid Mechanics*, 1008, A1.

Härter, J., Martínez, D. S., Poser, R., Weigand, B., & Lamanna, G. (2023). Coupling between a turbulent outer flow and an adjacent porous medium: High resolved Particle Image Velocimetry measurements. *Physics of Fluids*, 35(2). doi:10.1063/5.0132193

He, X., Apte, S., Schneider, K., & Kadoch, B. (2018). Angular multiscale statistics of turbulence in a porous bed. *Physical Review Fluids*, 3(8), 084501.

He, X., Apte, S. V., Finn, J. R., & Wood, B. D. (2019). Characteristics of turbulence in a face-centred cubic porous unit cell. *Journal of Fluid Mechanics*, 873, 608–645.

Hewitt, D. R., Neufeld, J. A., & Lister, J. R. (2012). Ultimate Regime of High Rayleigh Number Convection in a Porous Medium. *Physical Review Letters*, 108(22), 224503.

Huang, C.-W., Srikanth, V., & Kuznetsov, A. V. (2022). The evolution of turbulent micro-vortices and their effect on convection heat transfer in porous media. *Journal of Fluid Mechanics*, 942, A16.

Itoh, M., Tamano, S., Iguchi, R., ... Kubo, S. (2006). Turbulent drag reduction by the seal fur surface. *Physics of Fluids*, 18(6). doi:10.1063/1.2204849

Jin, Y., & Kuznetsov, A. V. (2017). Turbulence modeling for flows in wall bounded porous media: An analysis based on direct numerical simulations. *Physics of Fluids*, 29(4). doi:10.1063/1.4979062

Jin, Y., Uth, M.-F., Kuznetsov, A. V., & Herwig, H. (2015). Numerical investigation of the possibility of macroscopic turbulence in porous media: a direct numerical simulation study. *Journal of Fluid Mechanics*, 766, 76–103.

Kuwata, Y., & Suga, K. (2019). Extensive investigation of the influence of wall permeability on turbulence. *International Journal of Heat and Fluid Flow*, 80, 108465.

Manes, C., Poggi, D., & Ridolfi, L. (2011). Turbulent boundary layers over permeable walls: scaling and near-wall structure. *Journal of Fluid Mechanics*, 687, 141–170.

Mell, W., Maranghides, A., McDermott, R., & Manzello, S. L. (2009). Numerical simulation and experiments of burning douglas fir trees. *Combustion and Flame*, 156(10), 2023–2041.

Rajagopalan, R., & Tien, C. (1976). Trajectory analysis of deep-bed filtration with the sphere-in-cell porous media model. *AIChE Journal*, 22(3), 523–533.

Rao, F., & Jin, Y. (2022). Possibility for survival of macroscopic turbulence in porous media with high porosity. *Journal of Fluid Mechanics*, 937, A17.

Rosti, M. E., Brandt, L., & Pinelli, A. (2018). Turbulent channel flow over an anisotropic porous wall – drag increase and reduction. *Journal of Fluid Mechanics*, 842, 381–394.

Srikanth, V., Huang, C.-W., Su, T. S., & Kuznetsov, A. V. (2021). Symmetry breaking of turbulent flow in porous media composed of periodically arranged solid obstacles. *Journal of Fluid Mechanics*, 929, A2.

Srikanth, V., & Kuznetsov, A. V. (2025). Symmetry breaking of turbulent flow due to asymmetric vortex shedding in periodic porous media. *Physics of Fluids*, 37(6). doi:10.1063/5.0266758

Suga, K., Matsumura, Y., Ashitaka, Y., Tominaga, S., & Kaneda, M. (2010). Effects of wall permeability on turbulence. *International Journal of Heat and Fluid Flow*, 31(6), 974–984.

Uth, M.-F., Jin, Y., Kuznetsov, A. V., & Herwig, H. (2016). A direct numerical simulation study on the possibility of macroscopic turbulence in porous media: Effects of different solid matrix geometries, solid boundaries, and two porosity scales. *Physics of Fluids*, 28(6). doi:10.1063/1.4949549

Zamani, M., Sangtarash, A., & Javad Maghrebi, M. (2021). Numerical Study of Porous Media Effect on the Blade Surface of Vertical Axis Wind Turbine for Enhancement of Aerodynamic Performance. *Energy Conversion and Management*, 245, 114598.

Zhao, C. Y., & Lu, T. J. (2002). Analysis of microchannel heat sinks for electronics cooling. *International Journal of Heat and Mass Transfer*, 45(24), 4857–4869.